Nonisothermal Austenite Grain Growth Kinetics in a Microalloyed X80 Linepipe Steel

KUMKUM BANERJEE, MATTHIAS MILITZER, MICHEL PEREZ, and XIANG WANG

Nonisothermal austenite grain growth kinetics under the influence of several combinations of Nb, Ti, and Mo containing complex precipitates has been studied in a microalloyed linepipe steel. The goal of this study is the development of a grain growth model to predict the austenite grain size in the weld heat affected zone (HAZ). Electron microscopy investigations of the as-received steel proved the presence of Ti-rich, Nb-rich, and Mo-rich precipitates. The steel has then been subjected to austenitizing heat treatments to selected peak temperatures at various heating rates that are typical for thermal cycles in the HAZ. Thermal cycles have a strong effect on the final austenite grain size. Using a mean field approach, a model is proposed for the dissolution of Nb-rich precipitates. This model has been coupled to a Zener-type austenite grain growth model in the presence of pinning particles. This coupling leads to accurate prediction of the austenite grain size along the nonisothermal heating path simulating selected thermal profiles of the HAZ.

DOI: 10.1007/s11661-010-0376-2

I. INTRODUCTION

To transport natural gas from the gas fields to the consumers, long distance pipelines are used. For these pipelines, increasingly higher strength linepipe grades, *i.e.*, X80 and X100, are required to reduce the cost by thinner wall thickness and enhance the gas transportation efficiency by increased operating pressure.[1] In addition, novel welding procedures are crucial to produce high-quality welds that allow safe operation of the pipeline but that also enable cost efficient welding in the field. Controlled hot rolling and accelerated cooling are usually employed for producing linepipe steels. Weld strength is a dominating factor in assessing the overall performance of these materials for the manufacturing of pipelines, which, to a large degree, is controlled by the austenite grain size in the heat affected zone (HAZ). Large austenite grains near the fusion line may promote the formation of martensitic or bainitic transformation products with adverse effects on weld properties, *e.g.*, fracture toughness.[2–4] For example, Hamad *et al.*[4] found that maintaining a relatively fine austenite grain size in the HAZ is critical to enhance the crack tip opening displacement (CTOD) values such that a minimum target CTOD value of 0.15 mm at 253 K (20 °C) can be realized in X80 linepipe steels. Thus, reducing the migration rates of austenite grain boundaries during welding, with an aim of achieving fine austenite grains, is an important metallurgical phenomenon to control the resultant properties favorably in high strength microalloyed steels. Finely dispersed particles impose pinning forces that restrict the boundary movement and grain growth during heat treatment or welding.[5–9] Sufficiently finely dispersed particles containing the microalloying elements, niobium, titanium, or vanadium, have been found to inhibit austenite grain growth effectively.[6,10–13] During welding, particle dissolution or coarsening may occur in the HAZ depending upon the thermal cycle. The associated change in average particle size and volume fraction reduces the pinning force and may, thus, play a crucial role in controlling the austenite grain size in the HAZ.[13,14] A plethora of research work has been carried out on austenitization and the control of the grain size for more than 50 years.[6,11,12,15–20] It is well known that higher temperatures favor grain growth.[19] The role of heating rate and nonisothermal heat treatment cycles is less clear—significant effects on grain growth have been observed that cannot be concluded from isothermal studies.[21–24] An extensive review of the literature by Mishra and DebRoy[24] provides an overview of grain growth characteristics under significant spatial and temporal variations that are relevant for the HAZ.

An important aspect of HAZ grain structures is the presence of large grains in the grain-coarsened portion of the HAZ adjacent to the fusion line where the material is exposed to the thermal cycle with the highest peak temperature. Minimizing the grain size in this grain-coarsened region appears to be critical in mitigating the detrimental effects on mechanical properties. Thus, it is imperative to study austenite grain growth under extensively nonisothermal conditions employing the high heating rates that typically occur in the HAZ. Based on

KUMKUM BANERJEE, Researcher, is with the Research & Development Department, Tata Steel Ltd., Jamshedpur 831007, India. MATTHIAS MILITZER, Professor, is with The Centre for Metallurgical Process Engineering, The University of British Colombia, Vancouver, BC, Canada V6T 1Z4. Contact e-mail: matthias.militzer@ubc.ca MICHEL PEREZ, Professor, is with the Université de Lyon, INSA Lyon, MATEIS, UMR CNRS 5510, Lyon, France. XIANG WANG, Research Associate, is with the Materials Science and Engineering Department, McMaster University, Hamilton, ON, Canada L8S 4L7.

Manuscript submitted March 29, 2010.

Published online: 10 August 2010

these studies, grain growth models can be developed that are applicable to predict the grain structure in the HAZ as a function of heating rate and peak temperature. Such models would provide the pipeline manufacturers with a tool to assess suitable operating windows for welding procedures of a given steel.

To date, a number of empirical and more fundamental models have been developed for predicting austenite grain growth considering the effect of alloying elements.[13–17,19,22] However, most of these models are limited to isothermal situations. In recent years, models have been extended to grain growth under nonisothermal conditions.[13,21] Even though progress has been made in the investigation of various aspects of nonisothermal grain growth in metals and alloys, further advances are required in the understanding of this subject.

In the present work, nonisothermal austenite formation and austenite grain growth have been investigated at high heating rates to various austenitization temperatures in an X80 linepipe steel. In addition to microstructural characterization by conventional metallographic techniques, the evolution of the particle size distribution has been investigated by transmission electron microscopy. Based on the experimental data, a phenomenological model for nonisothermal austenite grain growth kinetics is proposed taking into account the dissolution kinetics of precipitates. The dissolution model is coupled to the grain growth model *via* a Zener-type pinning force that depends on particle radius and volume fraction.

II. MATERIAL AND TREATMENTS

The studies were carried out on a Nb-Ti-Mo microalloyed X80 steel supplied by the Canadian steel manufacturer, Evraz Inc. NA (Regina, SK). The as-received steel was in the pipe form with 16.9-mm gage. The chemical composition of the investigated steel is reported in Table I in terms of the key alloying elements.

Data provided from welding trials at Evraz Inc. NA indicate that heating rates in the HAZ can be in excess of 1000 K/s for typical girth weld procedures using single or dual torch submerged arc welding. To simulate austenitization and grain growth for these conditions in the laboratory, a Gleeble 3500 thermomechanical simulator (Dynamic Systems Inc., Poestenkill, NY) was employed. Here, the heating rates that could be attained were restricted to a maximum of 1000 K/s. To achieve these high heating rates, sheet samples were employed with a thickness of 0.6 mm, a length of 60 mm, and a width of 10 mm. The samples were heated at a particular heating rate (10, 100, or 1000 K/s) to an austenitization temperature of 1223 K, 1423 K, or 1623 K (950 °C, 1150 °C, or 1350 °C) followed by either (1) rapid quenching using water or (2) cooling at 100 K/s to 1173 K (900 °C) before quenching to mimic typical thermal profiles of the HAZ. The tests were performed in an argon atmosphere that was attained after high vacuum ($0.26\ \text{Pa} = 2 \times 10^{-3}$ Torr) was established before backfilling the chamber with argon. Figure 1 illustrates schematically the employed thermal profiles. The holding time at peak temperatures before quenching or cooling has been estimated to be 0.5 seconds. The temperature was controlled using an S-type (Pt/Rh-Pt) thermocouple spot welded at the center of the sample.

Table I. Chemical Composition (Key Alloying Elements) of the X80 Steel

	C	Mn	Nb	Ti	Mo	N
(wt pct)	0.06	1.65	0.034	0.012	0.24	0.005
(at. pct)	0.28	1.7	0.020	0.014	0.14	0.020

III. EXPERIMENTAL TECHNIQUES

A. *Dilatometry*

To record the austenite formation kinetics during continuous heating, a dilatometer was attached onto the sample and the dimensional change was measured in the width direction. The peak temperatures were 1623 K and 1423 K (1350 °C and 1150 °C) for the dilatometric tests. These tests were conducted under the high vacuum condition and samples were air cooled after the peak temperature had been reached. The volume fraction of austenite was determined as a function of temperature using the lever rule when the dilatometer response deviates from the linear portions of thermal expansion of single-phase ferrite and austenite, respectively.

B. *Metallography*

1. *Austenite grain size measurement*

To measure the austenite grain size metallographically, it is essential to reveal the austenite microstructure in the as-quenched samples. For this purpose, the thermally cycled samples were cut and tempered at 773 K (500 °C) in a tube furnace in the presence of argon for 24 hours to allow the segregation of elements such as P and S on the grain boundaries to improve the response of the grain boundaries to etching.[25–27] Subsequently, the through-thickness section of the quenched and tempered samples was ground and polished using conventional metallographic techniques. The austenite grain boundaries were

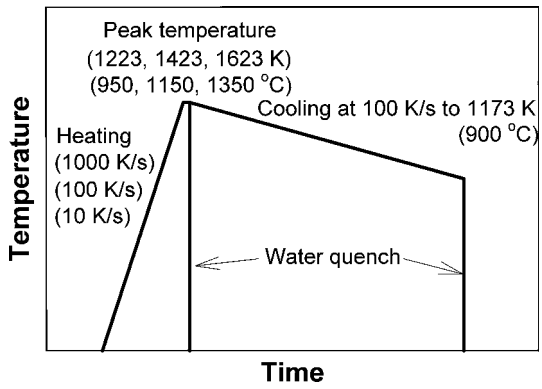

Fig. 1—Schematics of thermal profiles realized with the Gleeble thermomechanical simulator.

revealed using 4 g of sodium dodecylbenzene sulfonic acid in 100 mL of saturated aqueous picric acid diluted in 100 mL of distilled water in the presence of a few drops of Triton X-100 surface active reagent (Sigma-Aldrich, St. Louis, MO).[28] The optimized temperature and time for etching were between 333 K and 343 K (60 °C and 70 °C) and 60 to 180 seconds, respectively.

Polished and etched samples were photographed using an optical microscope. Then, the revealed austenite grain boundaries were traced and subsequently scanned. The tracings were analyzed for the mean grain area using Clemex image analyzing software (Clemex Technologies Inc., Longueuil, PQ, Canada). The area of each grain was defined as the sum of its net internal area and half the area of its boundary, so that the pixels used by the grain boundaries could be incorporated while calculating the area of a grain. The image analysis did not take into account incomplete grains that were intercepted by the frame of the field of measurement. From the grain area, A, the equivalent area diameter (EQAD), d_A, was calculated using the relation

$$d_A = \sqrt{\frac{4A}{\pi}} \qquad [1]$$

The mean EQAD was obtained by using the mean grain area in Eq. [1]. The true mean volumetric grain size, d_m, is then obtained by multiplying the mean EQAD by 1.2, as proposed by Giumelli *et al.*[18]

2. *Precipitate analysis*

The precipitates were analyzed in the as-received material and in samples heated at 10 K/s to peak temperatures of 1223 K, 1423 K, and 1623 K (950 °C, 1150 °C, and 1350 °C), respectively. These samples were then quenched by helium to room temperature. The microstructures of the as-received steel were investigated by optical microscopy, scanning electron microscopy (SEM), and transmission electron microscopy (TEM). Standard techniques with 2 pct nital etching were used for optical and SEM micrography to examine the ferrite microstructure. A Hitachi S-2300 (Hitachi Science Systems Ltd., Tokyo, Japan) was used for SEM studies.

To analyze the precipitates, various TEM techniques were employed. Both thin foils and replica studies were performed. For the thin foil studies, foils were prepared by cutting from the sample and grinding to less than 0.8 mm in thickness. Discs were punched from the wafers and electropolished using a solution of 10 pct perchloric acid and 90 pct methanol. Foils were examined by a conventional transmission electron microscope, PHILIPS* CM-12, operated at 120 keV and equipped with a LINK energy-dispersive X-ray (EDX) system (Oxford-ISIS, Ottawa, ON, Canada) for chemical analysis. The precipitates in different samples were characterized in terms of size, morphology, and chemistry by EDX for relatively large precipitates (>10 nm) and crystallography by a selected area diffraction pattern (SADP).

*PHILIPS is a trademark of Philips Electronic Instruments Corp., FEI Company, Hillsboro, OR.

To obtain statistically more relevant data on initial particle size, distribution and chemistry replica studies were performed for the as-received steel. For this purpose, the polished specimens were lightly etched in 2 pct nital. Subsequently a thin carbon film was deposited on the specimen and extracted using a solution of 10 mL of nitric acid in 90 mL of ethanol, followed by thoroughly cleaning the replicas in distilled water. The replicas were collected using 400-mesh copper grids before examination by TEM. The precipitates in these collected replicas were examined chemically using a Hitachi H-800 scanning transmission electron microscope (STEM) operated at 100 keV with EDX analysis using Quartz XONE8 software (Quartz Imaging Corp., Vancouver, BC, Canada).

IV. EXPERIMENTAL RESULTS

A. *As-Received Material*

1. *Microstructure*

Representative optical, SEM, and TEM micrographs of the as-received steel are presented in Figure 2. The microstructure is predominantly a fine ferritic structure (Figure 2(a)), which is complex and consists of non-equiaxed and acicular ferrite in association with martensite-austenite (MA) constituents (Figure 2(b)). Furthermore, at places, pockets of bainitic structures were also noted, as indicated by circles in Figure 2(b). As seen in the TEM micrograph of Figure 2(c), the ferrite structure is indeed highly dislocated.

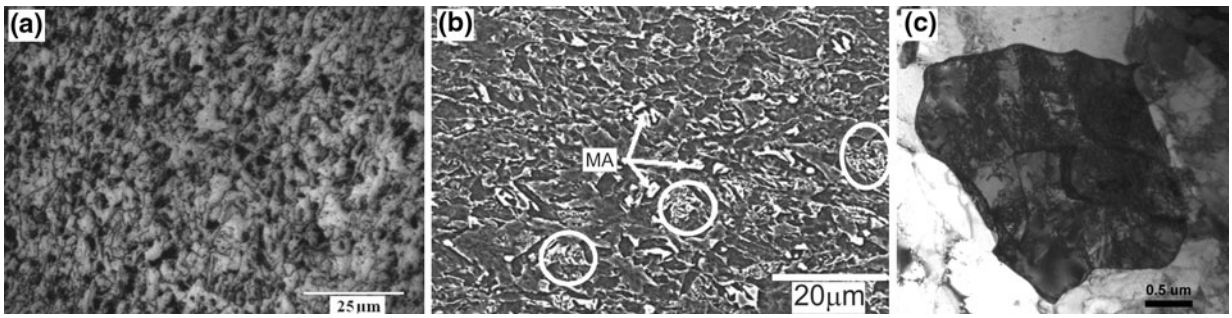

Fig. 2—Micrographs of as-received X80 steel: (*a*) optical micrograph, (*b*) SEM micrograph showing MA constituents and bainitic pockets (encircled), and (*c*) TEM micrograph of highly dislocated ferrite.

2. *Precipitates*

Figure 3 shows representative bright-field TEM micrographs of the as-received steel. There are a variety of Ti, Nb, and Mo containing precipitates with sizes (in terms of radius) ranging from 1 to 200 nm. The first type of precipitates is cuboidal in shape, and sizes were typically in the range of 20 to 100 nm. They are randomly distributed within grains. These precipitates have been identified as TiN according to their diffraction pattern. EDX spectra made from carbon replicas confirmed these particles as Ti rich (Figure 4). The Cu peaks in the EDX spectra correspond to the copper mesh that supports the replica. As indicated in Figure 3(a), these precipitates may contain a small amount of Nb. In addition to Ti-rich particles, a second family of coarse precipitates has been observed with irregular shape and sizes in the range of 5 to 100 nm. Figure 3(a) gives an example of one of these precipitates. As indicated there, most of these precipitates are confirmed as Nb-rich carbonitrides (NbCN), but a small amount of them is Mo_2C. Some of the Nb-rich precipitates are located at grain boundaries.

Figures 3(b) and (c) show the very fine precipitates that are to a great extent observed within the grains, and their radii are in the range of 1 to 3 nm. They are homogeneously distributed within grains (Figure 3(b)) and frequently found on dislocations (Figure 3(c)) and subgrain boundaries. These precipitates have been identified by SADP as a mixture of NbCN with small amounts of Mo_2C as evaluated by frequency and strength of appearance of reflections from NbCN or Mo_2C. The analysis of the diffraction pattern indicated that the 001 ferrite zone axis was parallel to the 011 zone axis of NbCN precipitates.

A more statistically relevant analysis of particle chemistries has been performed with carbon replicas for precipitates with sizes >10 nm; *i.e.*, it was challenging to observe the fine precipitates using the replica technique. Each precipitate was analyzed with respect to its composition (atomic percent) and radius (nanometer). Various combinations of complex precipitates have been recorded including Ti-rich-Nb-Mo (with atomic ratios of 45:4:1) Nb-rich-Ti-Mo (27:5:1) Nb-rich-Mo (9:1), and Ti-rich-Nb (5:1) in addition to precipitates that primarily contain just one of the elements, *i.e.*, Ti, Nb, or Mo. Thus, the coarser precipitates can be broadly divided into three families: Ti-rich (TiN), Nb-rich (NbCN), and Mo-rich (Mo_2C) precipitates. The combined precipitate size distribution including all three families is shown in Figure 5. The contributions of the three microalloying elements to each size class are indicated. From the overall precipitate volume of each precipitate family, it is determined that Ti-rich precipitates amount to 61 pct of the observed large precipitates, Nb-rich precipitates to 23 pct, and Mo-rich precipitates to 16 pct.

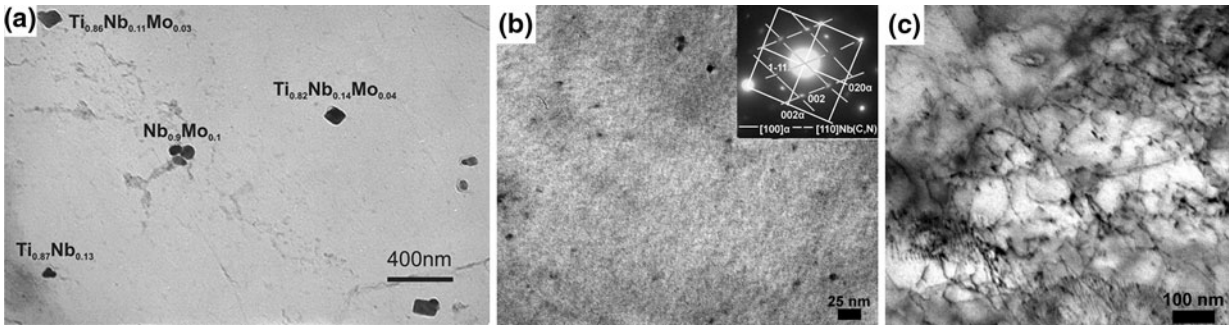

Fig. 3—Bright-field TEM micrographs of the as-received X80 steel showing (*a*) coarser Ti- and Nb-rich precipitates indicating their composition as obtained from EDX spectra, (*b*) fine precipitates identified as NbCN by diffraction pattern (inset), and (*c*) very fine precipitates on dislocations.

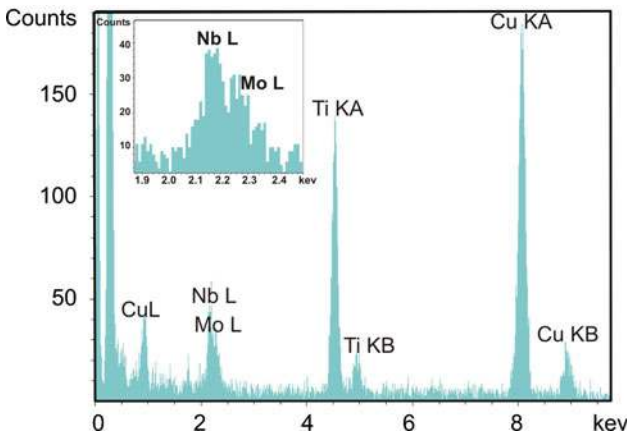

Fig. 4—EDX spectra of Ti-rich cuboidal particles.

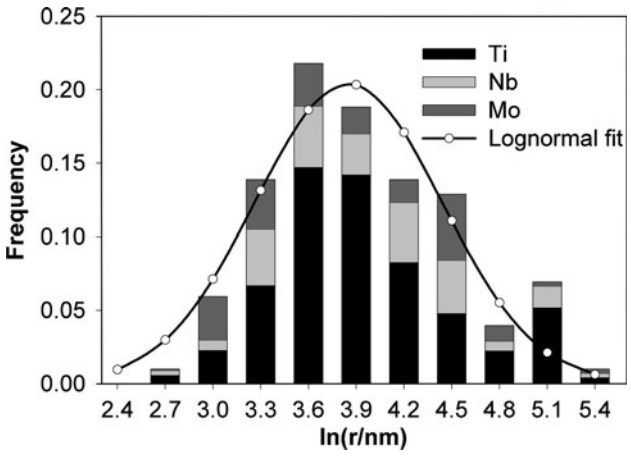

Fig. 5—Precipitate size distribution for coarser precipitates.

As illustrated in Figure 5, the measured precipitate size distribution can be well represented by a log-normal distribution:

$$v(r) = \frac{1}{\sqrt{2\pi}sr}\exp\left(-\frac{[\ln(r/\mu)]^2}{2s^2}\right) \quad [2]$$

where $v(r)$ is the probability density of a log-normal particle size distribution, r is the individual particle radius, μ is the median radius (here: 47 nm) of the distribution, and s is the standard deviation (here: 0.58). The average radius of the Ti-rich, Nb-rich, and Mo-rich precipitates is 61, 69, and 53 nm, respectively.

The detailed investigation of the precipitate state of the as-received material is critical, as this is the initial state for the potential dissolution and coarsening of precipitates during heating and the associated evolution of pinning austenite grain boundaries that greatly affects the resulting austenitic grain growth kinetics.

B. *Austenite Formation*

During continuous heating tests, the ferrite to austenite transformation kinetics have been determined by dilatometry for heating rates of 10, 100, and 1000 K/s, as shown in Figure 6. Table II summarizes the observed start (AC_1) and stop (AC_3) temperatures for austenite formation. The austenite formation temperatures increase with heating rate. The change of transformation temperatures is marginal when the heating rate is increased from 10 to 100 K/s. However, the start temperature increases by 20 and the finish temperature by 30 K when the heating rate is further increased from 100 to 1000 K/s. However, even for the highest heating rate studied here, austenite formation is completed at approximately 1183 K (910 °C), *i.e.*, well below the minimum peak temperature of 1223 K (950 °C) employed for subsequent austenite grain growth tests.

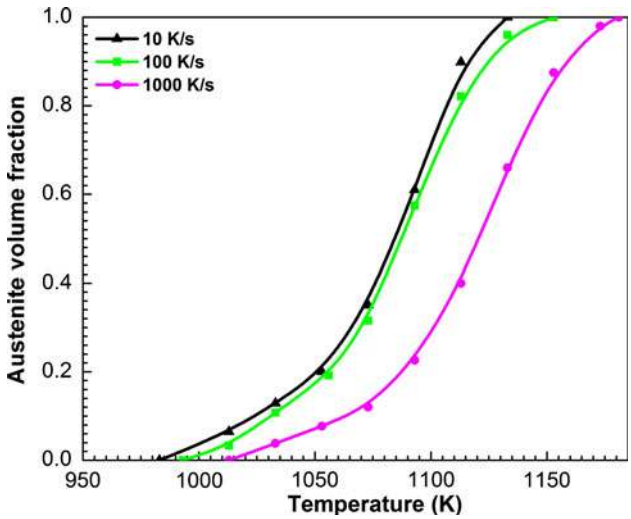

Fig. 6—Austenite formation kinetics at different heating rates for the as-received X80 steel under continuous heating conditions.

C. *Austenite Grain Growth*

Figure 7 displays the optical micrographs showing the prior austenite microstructures for the continuous heating tests with rates of 10, 100, and 1000 K/s to peak temperatures of 1223 K, 1423 K, and 1623 K (950 °C, 1150 °C, and 1350 °C). These micrographs permit a reasonably accurate tracing of the austenite grain boundaries and, thus, austenite grain size measurements. To have sufficient statistics and accuracy for the grain size distribution, the number of grains measured was in the range of 400 to 1700 (Table III).

As can be seen from the micrographs shown in Figure 7, a homogeneous distribution of grains is obtained for all conditions indicating that normal grain growth does take place. Then the grain structure can be characterized with a representative mean grain size. Table III shows the mean volumetric grain size obtained by multiplying the measured value of the mean EQAD by 1.2. The error of quantifying the average grain size has been estimated to be approximately 15 pct based on the accuracy at which austenite grain boundaries can be identified. Figure 8 summarizes the evolution of the mean volumetric grain size during continuous heating. As expected, increasing the peak temperature and decreasing the heating rate leads to larger grain sizes. Peak temperature has a dominant effect on the grain size, whereas heating rate plays a comparatively minor role. In particular, the grain size becomes independent of heating rates when they are sufficiently large, *i.e.*, here 100 K/s and higher. For these high rates, the heating times in austenite are comparable to the 0.5-second hold at the peak temperature before quenching. The heating times from 1173 K to 1623 K (900 °C to 1350 °C) are 4.5 seconds at 100 K/s and 0.45 seconds at 1000 K/s, respectively. The observed grain size is then primarily determined by the residence time at or near peak temperature. The mean austenite grain size at 1223 K (950 °C) is approximately 4 to 6 μm, and this can be viewed as the grain size resulting from the austenite formation. Increasing the peak temperature to 1423 K (1150 °C) leads to an increase of the grain size by a factor of approximately 2.5. Raising the peak temperature to 1623 K (1350 °C) increases further the grain sizes by a factor of 3 for the higher heating rates and a factor of 4 for 10 K/s.

Table II. Continuous Heating Transformation Temperatures for Different Heating Rates

Heating Rate, K/s	Peak Temperature	AC_1	AC_3
10	1623 K (1350 °C)	983 K (710 °C)	1133 K (860 °C)
100	1423 K (1150 °C)	994 K (721 °C)	1153 K (880 °C)
1000	1423 K (1150 °C)	1012 K (739 °C)	1181 K (908 °C)

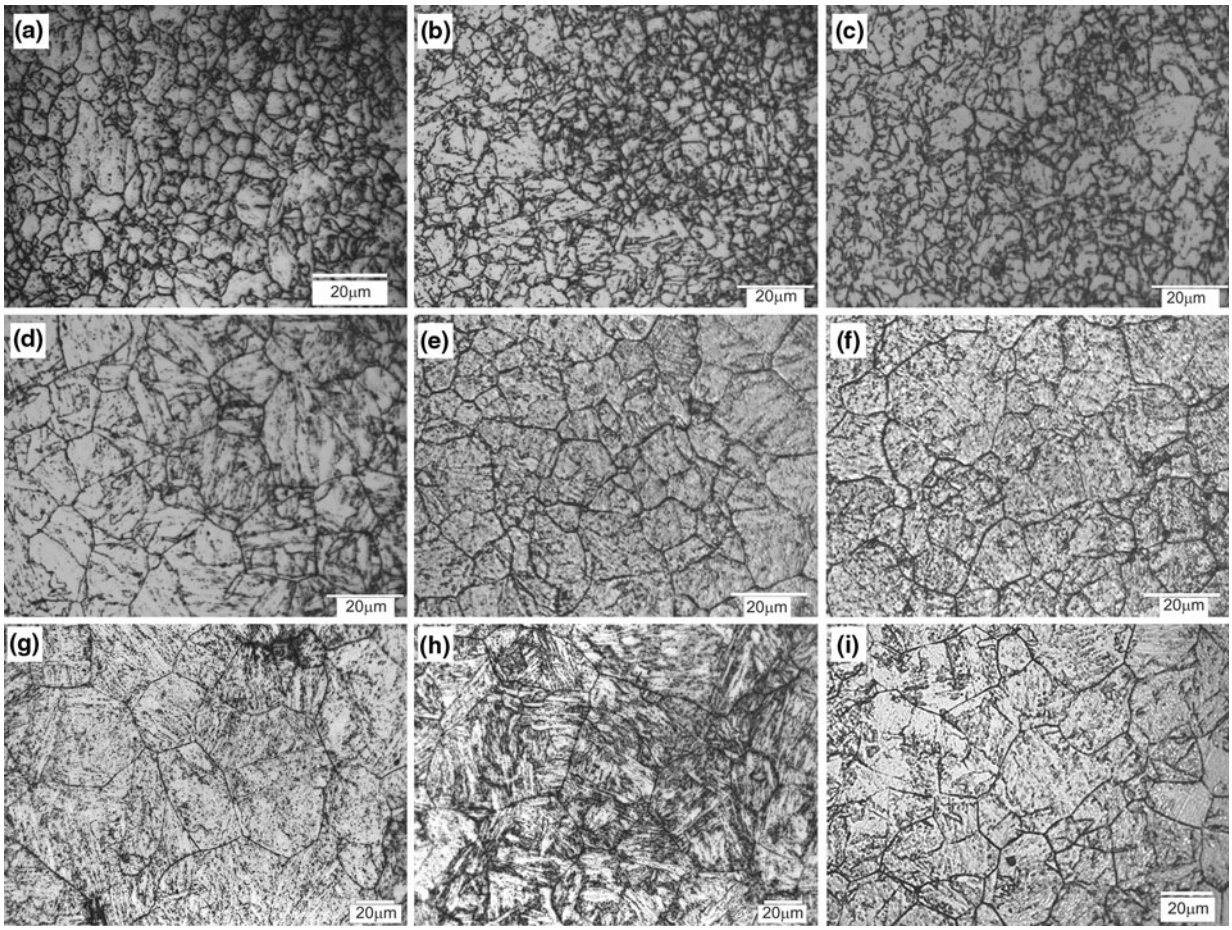

Fig. 7—Optical micrographs showing prior austenite grain boundaries for (*a*) through (*c*) 10, 100, and 1000 K/s heating rate to 1223 K (950 °C); (*d*) through (*f*) 10, 100, and 1000 K/s heating rate to 1423 K (1150 °C); and (*g*) through (*i*) 10, 100, and 1000 K/s heating rate to 1623 K (1350 °C).

Table III. Austenite Grain Size Measurement Data for Continuous Heating Tests

Peak Temperature	Heating Rate, K/s	Number of Grains	Mean Volumetric Grain Size (μm)	Standard Deviation
1223 K (950 °C)	10	1497	6.0	0.52
1223 K (950 °C)	100	1700	4.4	0.47
1223 K (950 °C)	1000	1741	4.2	0.51
1423 K (1150 °C)	10	670	15	0.60
1423 K (1150 °C)	100	839	11	0.54
1423 K (1150 °C)	1000	596	11	0.62
1623 K (1350 °C)	10	763	61	0.53
1623 K (1350 °C)	100	514	33	0.52
1623 K (1350 °C)	1000	428	32	0.42

For normal grain growth, the grain size distribution, $v(d)$, can usually be described with a log-normal distribution; *i.e.*,

$$v(d) = \frac{1}{\sqrt{2\pi}sd}\exp\left(-\frac{\left[\ln\left(d/d_g\right)\right]^2}{2s^2}\right) \qquad [3]$$

Here, s is the width of the distribution, d is the grain diameter, and d_g is the median grain diameter. Figure 9 provides an example for the observed grain size distributions using the measured EQADs. Table III summarizes the values for s, indicating that the width of the

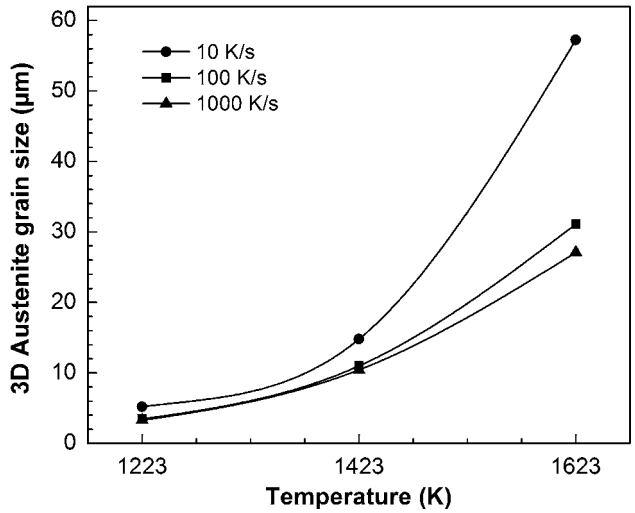

Fig. 8—Effect of heating rate on the mean volumetric austenite grain size.

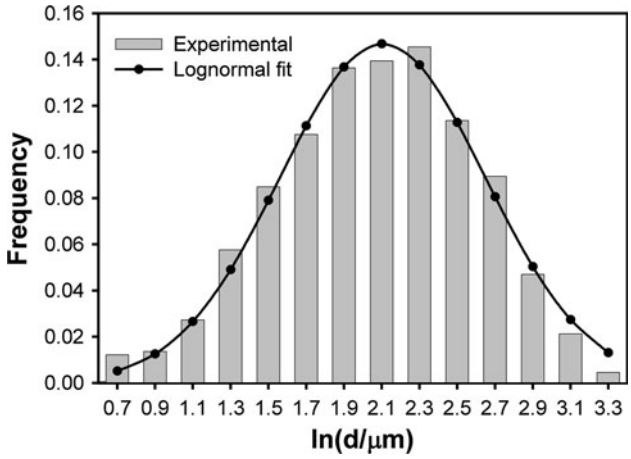

Fig. 9—Austenite grain size distribution for austenitizing temperature of 1423 K (1150 °C) and a heating rate of 100 K/s; solid line indicates fitted log-normal distribution.

grain size distribution is in a first approximation independent of heating conditions.

A number of tests were conducted to determine the extent of grain growth after cooling from the peak temperature to 1173 K (900 °C) at 100 K/s before water quenching. These thermal cycles represent typical temperature profiles at selected positions of the HAZ and, thus, provide more realistic information on the austenite grain size from which the austenite decomposition upon further cooling will occur. Figure 10 gives examples for the austenite microstructures obtained in these heating-cooling tests when the heating rate is 1000 K/s to peak temperatures of 1423 K and 1623 K (1150 °C and 1350 °C), respectively. For 1423 K (1150 °C), a marginal increase of the mean volumetric grain size from 11 to 15 μm is recorded during cooling, whereas this increase is more pronounced for 1623 K (1350 °C), *i.e.*, from 33 to 46 μm.

D. *Precipitate Evolution*

The evolution of the precipitate population was studied by TEM for samples continuously heated at 10 K/s to 1223 K, 1423 K, and 1623 K (950 °C, 1150 °C, and 1350 °C), respectively, before rapidly cooling to room temperature. In all samples, the large cuboidal TiN particles are observed as in the as-received material, thereby confirming the stability of these precipitates. There was no indication of coarsening, but after heating to the highest peak temperature of 1623 K (1350 °C), some smaller TiN are also observed with sizes below 10 nm. This may be taken as an indication of the onset of some very limited dissolution of TiN.

Significant changes have been observed in the populations of Mo- and Nb-rich particles. Already for the lowest peak temperature of 1223 K (950 °C), no Mo-rich precipitates are found anymore, suggesting dissolution of these particles that may even occur before austenite formation. Many irregular-shaped Nb-rich precipitates are present at 1223 K and 1423 K (950 °C and 1150 °C). However, the very fine precipitates that were numerous

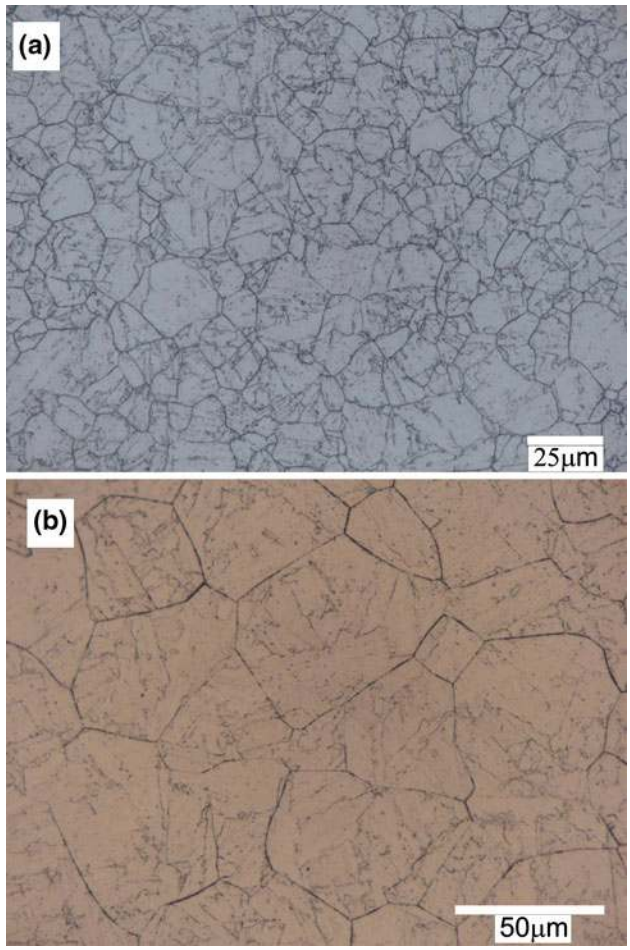

Fig. 10—Austenite microstructure after heating at 1000 K/s to peak temperatures of (*a*) 1423 K (1150 °C) and (*b*) 1623 K (1350 °C) and subsequent cooling at 100 K/s to 1173 K (900 °C) before water quench.

in the as-received material are not seen anymore. The minimum observed particle radius is 3.5 nm at both 1223 K and 1423 K (950 °C and 1150 °C), indicating that the fine particles have either undergone substantial coarsening or dissolution during heating. At 1623 K (1350 °C), almost no Nb-rich particles are observed, suggesting that complete dissolution of these particles takes place in the 1423 K to 1623 K (1150 °C to 1350 °C) temperature range for heating at 10 K/s.

V. MODELING

A. *Austenite Grain Growth Model*

The experimental observations confirm that austenite grain growth is affected by the presence of randomly distributed Nb- and Ti-rich precipitates. Significant dissolution of the Nb-rich particles will reduce pinning forces at higher temperatures, thereby promoting grain growth. Thus, a grain growth model must be developed that is linked to a dissolution model of the precipitates. These two models are linked by a pinning parameter. Grain boundary pinning was first analyzed by Zener

(Reference 29), and a Zener-type pinning approach is appropriate for the present situation.

In the presence of particles, the austenite grain growth rate can be expressed by

$$\frac{d}{dt}d_m = M(P_D - P_P) \quad [4]$$

where M is the mobility of the grain boundary, P_D is the driving pressure for grain growth, and P_P is the pinning pressure induced by precipitates. The grain boundary mobility, M, is given by

$$M = M_0 \exp\left(-\frac{Q}{\mathrm{R}T}\right) \quad [5]$$

where M_0 is a pre-exponential factor, Q is an activation energy, R is the gas constant, and T is the absolute temperature. The driving pressure can be expressed as[6]

$$P_D = \frac{4}{d_m}\gamma \quad [6]$$

where γ is the grain boundary energy. Zener derived a simple approach to estimate the pinning pressure; *i.e.*,[29]

$$P_Z = \frac{3f}{2r}\gamma \quad [7]$$

Here, f is the precipitate volume fraction and r the mean particle radius. By equaling driving (Eq. [6]) and pinning (Eq. [7]) pressures, Zener obtained the now classical expression for the critical grain size diameter, d_c:

$$\frac{d_C}{2} = \frac{4r}{3f} \quad [8]$$

More recently, based on many experimental results, Rios,[30] in agreement with Gladman,[6] proved a more accurate expression for the critical grain size to be 8 times smaller than Zener's. The pinning pressure, which will be considered in the model, is then in agreement with Rios:

$$P_P = 8P_Z = \frac{12f}{r}\gamma \quad [9]$$

Furthermore, in the case of the presence of different types of pinning particles, Eq. [9] can be rewritten as

$$P_P = 12\gamma \sum_i \frac{f_i}{r_i} \quad [10]$$

where the summation index i represents all present precipitate families. The analysis of precipitates in the investigated steel suggests consideration of three precipitate families: (1) Ti-rich particles considered to be TiN, (2) large Nb-rich particles, and (3) small Nb-rich particles. In a first approximation, the Nb-rich particles can be taken as NbCN as the Ti microalloying is insufficient to take all N out of solution. The Mo-rich particles that had been observed in the as-received material are not considered here, as they will already be in solution before reaching 1173 K (900 °C). Thermodynamic calculations using the TCFE5 database[31] confirm this assumption, which is consistent with the TEM observations in heat-treated samples. Then, Eq. [10] reads

$$P_P = 12\gamma\left(\frac{f_{\mathrm{TiN}}}{r_{\mathrm{TiN}}} + \frac{f_{\mathrm{NbCN}(s)}}{r_{\mathrm{NbCN}(s)}} + \frac{f_{\mathrm{NbCN}(l)}}{r_{\mathrm{NbCN}(l)}}\right) \quad [11]$$

where the indices (s) and (l) refer to the small and large NbCN precipitates, respectively.

B. *Precipitates Dissolution Model*

The dissolution of NbCN is considered in this model, whereas TiN dissolution can be neglected. The diffusion-controlled growth (or shrinkage) rate of spherical precipitates (molar composition X^P and radius r) embedded in a solid solution has been proposed by Zener[32] under the assumption of small supersaturation and local equilibrium. The rate controlling element is Nb and it is assumed that the fast diffusing interstitials (C, N) are homogeneously distributed in the matrix. Perez *et al.*[33] have shown that a mean radius approach is usually sufficient. Then the change in mean particle radii is obtained from

$$\frac{dr_j}{dt} = \frac{D}{r_j}\frac{X - X^j_{\mathrm{Nb}}(r_j)}{\alpha X^P - X^j_{\mathrm{Nb}}(r_j)} \quad [12]$$

where the superscript j is introduced to indicate the two NbCN precipitate types, *i.e.*, small (s) and large (l), respectively. The term D is the diffusivity of the rate controlling element (*i.e.*, here Nb), X is the mean solute mole fraction of Nb in the matrix, X^j_{Nb} is the equilibrium solute mole fraction of Nb at the precipitate/matrix interface, and $\alpha = v^M_{at}/v^P_{at}$ is the ratio of matrix to precipitate atomic volumes (mean volume per atom). Interface curvature plays an important role in equilibrium mole fraction, *i.e.*, the so-called Gibbs–Thomson effect, and the equilibrium solubility depends on particle radius, r_j, and the matrix/precipitate interface energy, σ, such that[34]

$$X^j_{\mathrm{Nb}}(r_j)X_{\mathrm{C+N}} = K_{\mathrm{NbCN}}\exp\left(\frac{4\sigma v^{\mathrm{NbCN}}_{at}}{r_j \mathrm{k_B} T}\right) \quad [13]$$

where $\mathrm{k_B}$ is the Boltzmann constant and K_{NbCN} is the solubility product. As NbCN (s) and NbCN (l) precipitates are considered, Eqs. [12] and [13] lead to a set of four coupled equations. The effective interstitial mole fraction is evaluated as follows. As nitrogen is much more stable in TiN than in NbCN, the nitrogen content can be divided into two parts, the first one being devoted to TiN precipitation and the second one available for precipitation of NbCN. From the initial composition of the alloy (denoted as X^o_{Ti}, X^o_{Nb}, X^o_{C}, and X^o_{N} and given in Table I), the atomic fraction of N required for the precipitation of TiN is $X^{\mathrm{Ti}}_{\mathrm{N}} = X^o_{\mathrm{Ti}}$, whereas the atomic fraction of C and N available for the precipitation of NbCN is $X^o_{\mathrm{C+N}} = X^o_{\mathrm{C}} + \left(X^o_{\mathrm{N}} - X^o_{\mathrm{Ti}}\right)$. Mass balance equations are used to

update, at each time-step, the amount of Nb and C + N in solid solution:

$$X_{\mathrm{Nb}} = X^{o}_{\mathrm{Nb}} - \frac{\alpha_{\mathrm{NbCN}}}{2}\left(f_{\mathrm{NbCN}(s)} + f_{\mathrm{NbCN}(l)}\right) \quad [14]$$

$$X_{\mathrm{C+N}} = X^{o}_{\mathrm{C+N}} - \frac{\alpha_{\mathrm{NbCN}}}{2}\left(f_{\mathrm{NbCN}(s)} + f_{\mathrm{NbCN}(l)}\right) \quad [15]$$

The volume fraction of each kind of precipitate can be calculated from the particle radius; *i.e.*,

$$f_j = n_j 4/3\pi r_j^3 \quad [16]$$

The particle densities n_j are determined from the initial particle size assuming that all microalloying elements are precipitated in the as-received steel.

C. *Model Parameters*

For the grain growth model, assumptions have to be made for the grain boundary properties. The grain boundary energy has been estimated to be 0.5 J/m^2. An activation energy of 350 kJ/mol for the grain boundary mobility has been taken from the work of Moon *et al.*[13] The pre-exponential mobility factor, M_0, is employed as the only adjustable parameter of the model.

For the dissolution model, the temperature dependence of diffusion and the solubility product need to be incorporated. Diffusivity of the microalloying elements in austenite is given by an Arrhenius relationship:

$$D = D_0 \exp\left(-\frac{Q_D}{\mathrm{R}T}\right) \quad [17]$$

where D_0 is the pre-exponential factor and Q_D is the activation energy. For diffusion of Nb in austenite, $D_0 = 1.50 \times 10^{-5}$ m^2/s and $Q_D = 345$ kJ/mol are taken.[35] The solubility product of NbCN is given by[36]

$$\log_{10} K_{\mathrm{NbCN}} = -\frac{6670}{T} - 1.32605 \quad [18]$$

Further, $\alpha_{\mathrm{NbCN}} = 1.05$ and a particle-matrix interfacial energy, σ, of 0.5 J/m^2 are employed.

Initial values for precipitate radii have been determined in the experimental investigations of the initial state (Section IV–A): $r^0_{\mathrm{NbCN}(s)} = 2$ nm and $r^0_{\mathrm{NbCN}(l)} = 69$ nm. The volume fraction of TiN precipitates can be estimated by assuming that all Ti is precipitated as TiN ($f_{\mathrm{TiN}} = 2.31 \times 10^{-4}$). From the ratio of the overall precipitate volumes in the as-received material for large NbCN (23 pct), TiN (61 pct), and Mo_2C (16 pct), an estimation of the initial volume fraction of large NbCN can be made:

$$f^0_{\mathrm{NbCN}(l)} = \frac{23}{61} f^0_{\mathrm{TiN}} = 8.71 \times 10^{-5} \quad [19]$$

The remaining carbonitrides are supposed to belong to the small NbCN family, leading to $f^0_{\mathrm{NbCN}(s)} = f^0_{\mathrm{NbCN}} - f^0_{\mathrm{NbCN}(l)} = 2.99 \times 10^{-4}$ when assuming equilibrium at 1173 K (900 °C). Then the initial precipitate number density, which remains constant during the simulation, can be directly estimated using $n_i = 3f_i^0/\left(4\pi\left(r_i^0\right)^3\right)$. Note that there are no fit parameters in the dissolution model.

D. *Simulation Results*

The simulation results of the combined grain growth-dissolution model are first illustrated for the continuous heating cases to a peak temperature of 1623 K (1350 °C), as in these cases, substantial dissolution of the Nb-rich particles occurs. Figure 11 shows the predicted dissolution kinetics in terms of precipitate volume fraction along the heating ramp as well as the resulting austenite grain size evolution. A value of 120 m^4/(Js) has been determined for M_0 to reasonably replicate the measured grain sizes. Considering the dissolution, it can be seen that the fine precipitates dissolve completely, whereas the coarse precipitates dissolve only completely at the lower heating rate of 10 K/s. This prediction is in agreement with the TEM observations (Section IV-D). The dissolution temperature of the fine precipitates increases with heating rate, *i.e.*, from approximately 1323 K (1050 °C) at 10 K/s to approximately 1473 K (1200 °C) at 1000 K/s. Austenite grain growth is predicted to only commence once these fine precipitates dissolve. This is an expected result as the fine precipitates exert an extraordinary pinning effect. For the assumed initial particle radius (2 nm) and volume fraction (3×10^{-4}), the limiting grain size is 2 μm, *i.e.*, smaller than the initial grain size that has resulted from austenite formation. As a result, the vast majority of grain growth occurs for 1000 K/s during the brief holding of 0.5 seconds at the peak temperature of 1623 K (1350 °C) (Figure 11(f)). For the lowest heating rate, grain growth occurs much more gradually during the heating stage rather than at the peak temperature (Figure 11(d)). The grain growth simulations clearly show that the observed increase of grain size with heating rate and peak temperature is not just a simple temperature effect due to the increase in the grain boundary mobility, but grain growth is critically augmented by the decrease in pinning pressure due to precipitate dissolution. Figure 12 provides a summary of the simulated and measured austenite grain sizes as a function of heating rate and peak temperature. Considering that just one adjustable parameter is used, an excellent agreement with the measured data is obtained.

More complex thermal profiles have been investigated in order to mimic more realistic welding treatments. Figure 13 shows the predicted evolution of the mean austenite grain size during three thermal cycles that involve cooling from the peak temperature to 1173 K (900 °C) at 100 K/s. The three heating ramps are (1) heating at 1000 K/s to 1623 K (1350 °C), (2) heating at 1000 K/s to 1423 K (1150 °C), and (3) heating at 100 K/s to 1423 K (1150 °C). The experimentally measured final austenite grain sizes are indicated for comparison. Again, good agreement is obtained between measured and predicted grain sizes. Significant grain growth

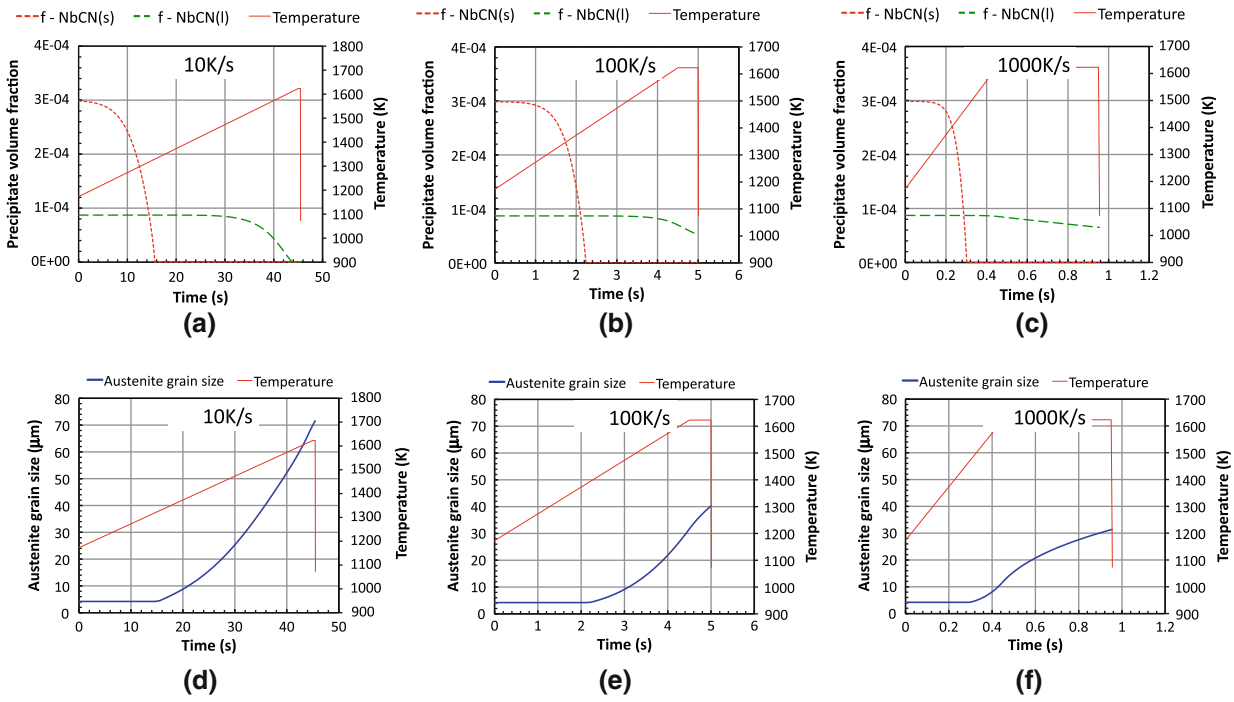

Fig. 11—(*a*) through (*c*) Predicted precipitate volume fraction and (*d*) through (*f*) simulated austenite grain size evolution during three heating ramps at (*a*) and (*d*) 10, (*b*) and (*e*) 100, and (*c*) and (*f*) 1000 K/s up to an austenitization temperature of 1623 K (1350 °C) followed by a hold of 0.5 s.

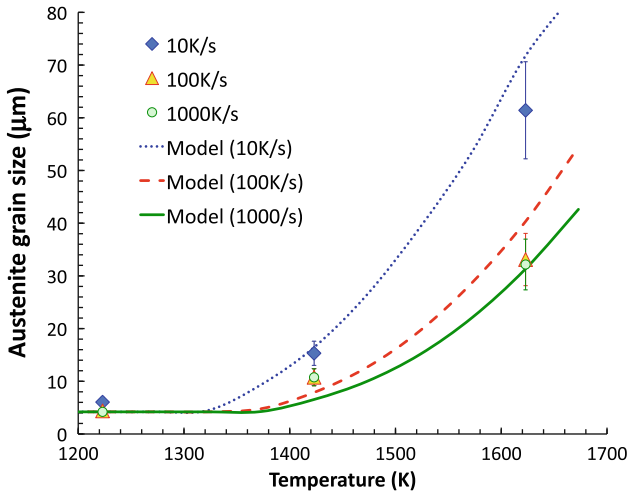

Fig. 12—Comparison between measured and simulated mean austenite grain sizes for continuous heating treatments.

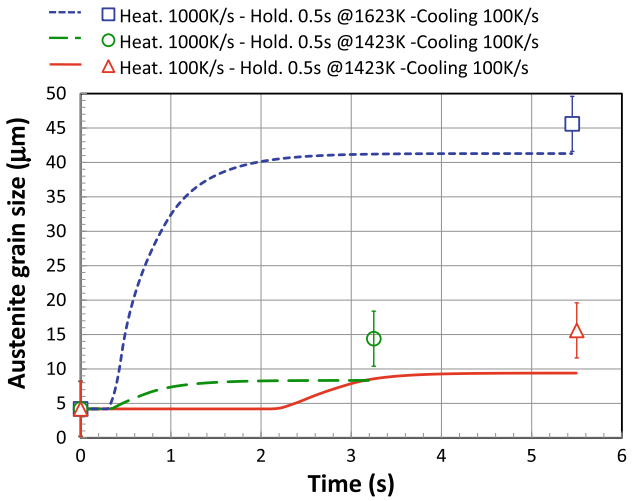

Fig. 13—Comparison between measured and simulated austenite grain size for thermal cycles involving heating and cooling.

during cooling is only predicted when the peak temperature is 1623 K (1350 °C), *i.e.*, from approximately 30 to 40 µm. This is enabled by the fact that only for this high peak temperature condition all fine precipitates are dissolved.

VI. DISCUSSION

A rather pragmatic phenomenological austenite grain growth model is proposed for thermal cycles that are typical for the HAZ in steels. It was possible to make a number of simplifying assumptions for a potentially complex metallurgical problem. Even though a number of precipitates dissolve during the rapid heating cycles, no abnormal grain growth is observed. Thus, the grain size evolution can be just described with a representative mean value. The absence of abnormal grain growth may be attributable to the rapid heating conditions. Using thermodynamic and diffusion data from the literature, fine Nb-rich precipitates are predicted to dissolve very rapidly once a sufficiently high-temperature region is

reached. For a heating rate of 1000 K/s, dissolution times are just fractions of a second. Such short dissolution times appear to prevent the formation of bimodal grain size distributions that are otherwise frequently observed in standard isothermal grain growth tests that are conducted in the dissolution temperature range. Considering that typical migration rates of grain boundaries may be on the order of micrometers per second, maximum migration distances during dissolution times may be less than a micrometer. In essence, a sharp transition from strongly pinned to weakly pinned grain growth occurs during rapid heating. One may propose to describe this transition in a first approximation with a dissolution temperature that is a function of heating rate.

Another important simplification that has been made is that just mean particle sizes of the as-received steel, *i.e.*, the base metal, have been used as input into the dissolution model. Neither particle size distributions nor particle coarsening are considered even though some indications of coarsening of the fine Nb-rich particles have been concluded from the TEM studies of samples heated at 10 K/s. This simplification leads to an underprediction of grain growth for lower temperatures; *i.e.*, simulated grain sizes for the 1423 K (1150 °C) peak temperature are smaller than the measured grain sizes, since for a given volume fraction, finer precipitates exert a larger pinning pressure. However, a number of assumptions would have to be made to predict particle coarsening in the HAZ. Coarsening rates in ferrite may be substantially augmented by fast diffusion along dislocations and subgrain boundaries. However, while coarsening during heating at 10 K/s may be appreciable, *i.e.*, increase of minimum particle radius from 1 to 3.5 nm, this effect will be much smaller for heating at 1000 K/s, which is more relevant for the HAZ. Further, predicted dissolution temperatures would somewhat increase with precipitate radius, *e.g.*, from 1473 K (1200 °C) for 2 nm to 1543 K (1270 °C) for 4 nm during heating at 1000 K/s.

The advantages of the proposed approach outweigh by far the potential drawbacks of the simplifying assumptions. The dissolution model is based on literature data and takes into account the precipitate types and sizes of the base metal eliminating the introduction of any fit parameters related to precipitation coarsening. The particle pinning pressure is calculated from the dissolution model, and this provides the coupling to a grain growth model describing the mean grain size. Using the grain boundary mobility as a fitting parameter, the model is calibrated to describe quantitatively the grain sizes observed for peak temperatures near the fusion line, in the present study 1623 K (1350 °C). To translate this model into a tool that can predict the grain size evolution in the HAZ, one will have to consider the thermal cycles in each position and the associated spatial temperature gradients. This can be accomplished with mesoscale models using Monte Carlo techniques or phase field modeling.[37,38] Explicit consideration of spatial temperature gradients is critical to account for the so-called thermal pinning effect, *i.e.*, grains in a homogenous temperature field will grow quicker than grains in a temperature gradient.[37]

VII. CONCLUSIONS

Nonisothermal austenite grain growth has been investigated in a Nb-Ti-Mo microalloyed X80 linepipe steel for heating conditions that are typical for the HAZ. In addition to austenite grain growth, the precipitate evolution has been studied. It has been found that rapid dissolution of Nb-rich particles enables grain growth above the dissolution temperature. For heating rates larger than 100 K/s, the austenite grain size is primarily a function of the peak temperature and rather independent of heating rate.

Based on the experimental observations, a rather pragmatic phenomenological austenite grain growth model is proposed that is coupled to a dissolution model for Nb-rich precipitates. Mo-rich precipitates are assumed to dissolve in ferrite and TiN is assumed to have a stable particle size distribution. The dissolution model requires information on mean particle sizes observed in the base metal and predicts then dissolution temperatures for each particle family using thermodynamic and diffusion data from the literature. Particle dissolution leads to a decrease of the pinning pressure for grain growth. The austenite grain growth kinetics is then described by just using the grain boundary mobility as a fit parameter. A very good agreement between measured and simulated grain sizes is observed for many different thermal conditions.

The combination of a dissolution model with a grain growth model gives a better understanding of the causes of austenite grain growth: it is due to a complex combination of kinetic (mobility of grain boundary) and thermodynamic (precipitate stability) aspects, which can hardly be individually observed during a welding cycle.

ACKNOWLEDGMENTS

The authors acknowledge the Natural Sciences and Engineering Research Council of Canada (NSERC), Evraz Inc. NA, and TransCanada Pipelines Ltd. for their financial support. We are also grateful to W.J. Poole for valuable discussions and suggestions. We thank H. Azizi-Alizamini, A. Meharwal, and M. Maalekian for their help with technical details of this work. One of the authors (MP) expresses his gratitude to Chad Sinclair and colleagues for their warm welcoming during a sabbatical stay at UBC from September 2008 to January 2009.

REFERENCES

1. I. Nobuyuki, E. Shigeru, and K. Joe: *JFE Techn. Rep.*, 2006, vol. 1, pp. 20–26.
2. N.J. Grant: *J. Met.*, 1983, vol. 35, pp. 20–27.
3. L.P. Zhang, C.L. Davis, and M. Strangwood: *Metall. Mater. Trans. A*, 1999, vol. 30A, pp. 2089–96.
4. F. Hamad, L. Collins, and R. Volkers: *Proc. 7th Int. Pipeline Conf. (IPC2008)*, ASME, Calgary, 2008, IPC2008-64097.
5. J. Gao, R.G. Thompson, and B.R. Patterson: *Acta Mater.*, 1997, vol. 45, pp. 3653–58.

6. T. Gladman: *The Physical Metallurgy of Microalloyed Steels*, The Institute of Materials, London, 2002, pp. 137–84.
7. D.W. Tian, L.P. Karjalainen, B.N. Qian, and X.F. Chen: *Metall. Mater. Trans. A*, 1996, vol. 27A, pp. 4031–38.
8. P.A. Manohar, M. Ferry, and T. Chandra: *ISIJ Int*., 1998, vol. 38, pp. 913–24.
9. M. Hillert: *Acta Metall*., 1988, vol. 36, pp. 3177–81.
10. P.A. Manohar, D.P. Dunne, T. Chandra, and C.R. Killmore: *ISIJ Int*., 1996, vol. 36, pp. 194–200.
11. T. Gladman: *Proc. R. Soc. London, Ser. A, Mathemat. Phys. Sci*., 1966, vol. 294, pp. 298–309.
12. T. Gladman and F.B. Pickering: *Iron Steel Inst. J*., 1967, vol. 205, pp. 653–64.
13. J. Moon, J. Lee, and C. Lee: *Mater. Sci. Eng. A*, 2007, vol. 459A, pp. 40–46.
14. H.R. Wang and W. Wang: *Mater. Sci. Technol*., 2008, vol. 24, pp. 228–32.
15. A. Yoshie, M. Fujioka, Y. Watanabe, K. Nishioka, and H. Morikawa: *ISIJ Int*., 1992, vol. 32, pp. 395–404.
16. Y. Saito and C. Shiga: *ISIJ Int*., 1992, vol. 32, pp. 414–22.
17. T. Senuma, M. Suehiro, and H. Yada: *ISIJ Int*., 1992, vol. 32, pp. 423–32.
18. A. Giumelli, M. Militzer, and E.B. Hawbolt: *ISIJ Int*., 1999, vol. 39, pp. 271–80.
19. S. Jiao, J. Penning, F. Leysen, Y. Houbaert, and E. Aernoudt: *ISIJ Int*., 2000, vol. 40, pp. 1035–40.
20. L. Dao, J. Wang, Q. Liu, X. Sun, and J. Cao: *J. Iron Steel Res. Int*., 2010, vol. 17, pp. 62–66.
21. S. Mishra and T. DebRoy: *Mater. Sci. Technol*., 2006, vol. 22, pp. 253–78.
22. M. Militzer, E.B. Hawbolt, T.R. Meadowcroft, and A. Giumelli: *Metall. Mater. Trans. A*, 1996, vol. 27A, pp. 3399–3409.
23. A. Danon, C. Servant, A. Alamo, and J.C. Brachet: *Mater. Sci. Eng. A*, 2003, vol. 348A, pp. 122–32.
24. S.S. Sahay, C.P. Malhotra, and A.M. Kolkhede: *Acta Mater*., 2003, vol. 51, pp. 339–46.
25. G.F. Vander Voort: *Metallography: Principles and Practice*, ASM INTERNATIONAL, Materials Park, OH, 1999, pp. 437–40.
26. G. Krauss: *Steels: Heat Treatment and Processing Principles*, ASM INTERNATIONAL, Materials Park, OH, 1989, pp. 188–97.
27. A. Sinha: *Ferrous Physical Metallurgy*, Butterworth Publishers, Stoneham, MA, 1989, pp. 574–77.
28. T. Gladman: *Heat Treatment of Metals (UK)*, 1994, vol. 21, pp. 11–14.
29. C. Zener: private communication to C.S. Smith, *Trans AIME*, 1948, vol.175, pp. 15–51.
30. P.R. Rios: *Acta Metall*., 1987, vol. 35, pp. 2805–14.
31. www.thermocalc.com.
32. C. Zener: *J. Appl. Phys*., 1949, vol. 20, pp. 950–53.
33. M. Perez, M. Dumont, and D. Acevedo: *Acta Mater*., 2008, vol. 56, pp. 2119–32.
34. M. Perez: *Scripta Mater*., 2005, vol. 52, pp. 709–12.
35. B. Sparke, K.W. James, and G.M. Leak: *J. Iron Steel Inst*., 1965, vol. 203, pp. 152–53.
36. K.J. Irvine, F.B. Pickering, and T. Gladman: *J. Iron Steel Inst*., 1967, vol. 205, pp. 161–82.
37. S. Mishra and T. DebRoy: *Acta Mater*., 2004, vol. 52, pp. 1183–92.
38. M. Toloui and M. Militzer: *Int. J. Mater. Res*., 2010, vol. 101, pp. 542–48.